Geomorphology 198 (2013) 189–200

Contents lists available at ScienceDirect

Geomorphology

journal homepage: www.elsevier.com/locate/geomorph

Modeling permafrost extension in a rock slope since the Last Glacial Maximum: Application to the large Séchilienne landslide (French Alps)

V. Lebrouc, S. Schwartz *, L. Baillet, D. Jongmans, J.F. Gamond

ISTerre, Université de Grenoble 1, CNRS, Grenoble F-38041, France

ARTICLE INFO

Article history:
Received 31 October 2012
Received in revised form 27 March 2013
Accepted 2 June 2013
Available online 10 June 2013

Keywords:
Permafrost modeling
TTOP model
Last Glacial Maximum
Large landslide
French Alps
Séchilienne

ABSTRACT

Recent dating performed on large landslides in the Alps has revealed that the initiation of instability did not immediately follow deglaciation but occurred several thousand years after ice down-wastage in the valleys. This result indicates that debuttressing is not the immediate cause of landslide initiation. The period of slope destabilization appears to coincide with the wetter and warmer Holocene Climatic Optimum, indicating a climatic cause of landslide triggering, although the role of seismic activity cannot be ruled out. A phenomenon which may partly explain the delay between valley deglaciation and gravitational instability is the temporal persistence of thick permafrost layers developed in the Alps since the Last Glacial Maximum (LGM). This hypothesis was tested through 2D thermal numerical modeling of the large Séchilienne landslide (Romanche valley, French Alps) using plausible input parameter values. Simulation results suggest that permafrost vanished in the Séchilienne slope at 10 to 11 ka, 3000 to 4000 years following the total ice down-wastage of the Romanche valley at 14.3 ka. Permafrost persistence could have contributed to the failure delay by temporally strengthening the slope. Numerical simulations also show that the permafrost depth expansion approximately fits the thickness of ground affected by gravitational destabilization, as deduced from geophysical investigations. These results further suggest that permafrost development, associated with an ice segregation mechanism, damaged the rock slope and influenced the resulting landslide geometry.

1. Introduction

The triggering of large gravitational movements in mountainous areas, following the last Pleistocene glacial retreat, has been a question debated for many years (see Sanchez et al., 2010 for a recent review). Glacial slope steepening and subsequent debutressing (lateral stress release resulting from ice melting) have been frequently proposed as major causes of rock-slope failures (Cruden and Hu, 1993; Augustinus, 1995; Cossart et al., 2008), although the role of other phenomena like cleft-water pressure, seismic activity and climatic changes have also been invoked (Ballantyne, 2002; Hormes et al., 2008; Ivy-Ochs et al., 2009; Le Roux et al., 2009). Local factors like relief and favorable fracture patterns also play a role in predisposing slopes to fail (Korup et al., 2007). In the last ten years, dating methods, mainly the ^{14}C and cosmic ray exposure (CRE) techniques, have provided chronological constraints on the failure time for major large alpine landslides (e.g., Bigot-Cormier et al., 2005; Deplazes et al., 2007; Ivy-Ochs et al., 2009; Le Roux et al., 2009; Prager et al., 2009). In the Alps, surface exposure age measurements in the above studies show that large landslides initiated around the early to mid-Holocene: Fernpass (Austria, 4.1 ka), Flims (Switzerland, 8.9 ka), Kandertal (Switzerland, 9.6 ka), Köfels (Austria, 9.8 ka), La Clapière (France, 10.3 ka), Séchilienne (France, 6.4 ka) and Valtellina (Italy, 7.4 ka). The time interval following total melting of ice in valleys during which the slope endures the new state of stress before the initiation of failure (pre-failure endurance; Ballantyne, 2002) was estimated at least between 2000 and 5400 years (Le Roux et al., 2009), implying that these events are not an immediate consequence of debutressing. Moreover, they often coincided with the Climatic Optimum period, which is characterized in the Alps by increased mean temperatures of 1–2 °C (Davis et al., 2003), forest cover density (de Beaulieu, 1977) and lake levels due to heavy annual precipitation (Magny, 2004, 2007). These data suggest that climatic changes play a major role in landslide triggering (Ivy-Ochs et al., 2009; Le Roux et al., 2009). Recently Sanchez al. (2010) applied the CRE technique on glacial, tectonic and gravitational surfaces in the SW Alps. The resulting dates of 11 to 8 ka clearly show that the main tectonic activity postdates deglaciation and corresponds to gravity destabilization. This interpretation is a probable consequence of the post-glacial rebound and the enhanced pore water pressure, the inferred cause of widespread slope fracturing. This tectonic phase was followed by rock weathering during the Climatic Optimum. The development of large gravitational mass movements could be related to the combined effects of intense tectonic activity and climatic change from cold and dry (Pleistocene) to warm and wetter (Holocene) phases. Although the validity of this scenario to the whole Alpine range has still to be documented, these results illustrate the complexity of the interaction among tectonic, climatic and gravitational processes. The

* Corresponding author. Tel.: +33 4 76 63 59 04; fax: +33 4 76 51 40 58.
E-mail address: Stephane.Schwartz@ujf-grenoble.fr (S. Schwartz).

0169-555X/$ – see front matter © 2013 Elsevier B.V. All rights reserved.
http://dx.doi.org/10.1016/j.geomorph.2013.06.001

question of the pre-failure endurance in the Canadian Rockies was addressed by Cruden and Hu (1993) who proposed an exhaustion model, which assumes that the overall probability of failure occurring within a given area diminishes exponentially with time elapsed since a deglaciation. As outlined by Ballantyne (2002), however, this model is difficult to calibrate and apply, particularly in zones characterized by gentle slopes.

Another factor that could contribute to explain pre-failure endurance is the persistence of permafrost in the rock mass. Indeed, a thick permafrost layer developed in the Alps during the Early Holocene, and probably reached more than 150 m deep as suggested by numerical modeling (Wegmann et al., 1998) and a permafrost/glacier evolution study (Guglielmin et al., 2001). The first effect of permafrost is to stabilize slopes by increasing mechanical properties. Comparing the deformation and strength properties of frozen and unfrozen crystalline rocks, Krivonogova (2009) has shown that the presence of ice increases the Young modulus and cohesion by a factor of about 2, while the friction angle remains similar. Permafrost development contributes to slope reinforcement, thus stabilizing surfaces. With significant variations of temperature over the last 21,000 years, permafrost thickness has varied with time disappearing in low-elevation slopes, similar to the one affected by the Séchilienne landslide in the French Alps, whose crown is at about 1100 m a.s.l. Ice disappearance has probably created favorable conditions for low-elevation slope failures, as suggested by the increasing evidence of destabilization at present (see Gruber and Haeberli, 2007 for a review). The sensitivity of permafrost to anthropomorphic climate change and its influence on natural hazards are now recognized, and numerical modeling is increasingly used for investigating the effect of climate variability and topography on permafrost temperature and extension (Riseborough et al., 2008; Noetzli and Gruber, 2009).

On the other hand, the presence of permafrost lasting millennia allowed the accumulation of ice-rich layers at the top and bottom of a frozen layer (Matsuoka et al., 1998), through the ice segregation mechanism. That occurs when liquid water migrates through a porous medium towards freezing surfaces, resulting from temperature gradient-induced suction in freezing or frozen ground (Murton et al., 2006). Laboratory experiments simulating rock freezing produce fractures containing segregated ice layers near the permafrost table (Murton et al., 2001). These results demonstrate that ice segregation is an important rock degradation process, as suggested by other authors (see Matsuoka and Murton, 2008 for a review). With permafrost boundary variations in rock slopes over long time-scales, ice segregation may have acted as a contributory factor producing rock mass fractures, preferentially parallel to the slope, to a depth of a few tens of meters or more (Matsuoka et al., 1998). Modeling the thermal evolution of the Konkordia ridge (Switzerland) since the end of the Little Ice Age, Wegmann et al. (1998) demonstrated permafrost penetration into the first decameters of rock as a consequence of temperate glacier retreat. Considering climatic variations in northern Fennoscandia and using the TTOP model (Temperature at the Top Of Permafrost; Riseborough et al., 2008) with constant *n*-factors, Kukkonen and Safanda (2001) showed that the permafrost thickness experienced considerable variations during the Holocene, with a maximum permafrost penetration between 100 and 250 m for low porosity rocks and temperate glacier conditions. In conclusion, they stressed that vegetation and snow cover changes during the Holocene should be taken into account in the model.

The present paper investigates the potential role of permafrost extension and persistence in the development of a large landslide during the period between deglaciation and failure initiation. The 2D thermal response of the Séchilienne slope (Western Alps, France) during the last 21,000 years was computed using the TTOP model for two scenarios: cold and temperate glaciers. The influence of long-term freeze-thaw action on slope fracturing was estimated by comparing the computed deeper permafrost extension with the present-day deconsolidated zone imaged by P-wave seismic tomography (Le Roux et al., 2011). The modeling has also permitted evaluation of the persistence effect of permafrost on slope evolution, in addition to the other involved processes like glacial debutressing and climatic change.

2. Geological and kinematic contexts

The lower Romanche valley is located in the Western Alps (southeast of France), about 20 km SE of Grenoble City (Fig. 1). It borders the southern part of the Belledonne massif (external crystalline massifs), which is divided into two main lithological domains, the external one to the west and the internal one to the east (Guillot et al., 2009). These two geological units are separated by a major Late Paleozoic near-vertical fault so-called Belledonne Middle Fault (BMF in Fig. 1). During the Quaternary, the Romanche Valley was subjected to many cycles of glaciation and deglaciation including the Last Glacial Maximum (LGM) around 21 ka (Clark et al., 2009) when the Romanche and Isère valleys were covered with ice to an elevation of 1200 m a.s.l (Montjuvent and Winistörfer, 1980) (Fig. 1). The relief of the lower Romanche valley shows a strong glacial imprint (van der Beek and Bourbon, 2008; Delunel et al., 2010; Le Roux et al., 2010) such as steep slopes dipping 35° to 40°, overdeepened troughs and glacial deposits. These characteristics suggest that the thermal regime of the glacier was temperate, although the majority of glaciers are polythermal (Owen et al., 2009). Moreover, the right bank of the Romanche valley is overlooked by a glacial plateau (the Mont Sec plateau) at an elevation higher than 1100 m a.s.l (Fig. 1). This plateau is locally overlain with relict peat bogs (Muller et al., 2007) that developed quickly in a cold and wet environment after the disappearance of ice. The steep slopes in the external domain of the Belledonne massif, which mainly consists of micaschists unconformably covered with Mesozoic sediments and Quaternary deposits, are affected by several active or dormant large gravitational movements (Fig. 1).

Among the observed movements, the best known and most active is the Séchilienne landslide (Fig. 1), whose 40 m high head scarp affects the southern edge of the Mont Sec glacial plateau (Fig. 2a). Below the head scarp, a moderately sloping depletion zone between 950 and 1100 m a.s.l exhibits a series of large depressions and salient blocks (Fig. 2a,c), while the lower part of the landslide, between 450 and 950 m a.s.l, shows steep convex slopes (>40°, Fig. 2c) and is interpreted as an accumulation zone (Vengeon, 1998). The Séchilienne slope is cut by three main sets of near-vertical open fractures oriented N20, N70 and N110 to N120 (Fig. 2b). This structural framework results in linear scarps and troughs filled by rock debris and topsoil (Fig. 2a), which delineate rock blocks displaying downslope motion. The N20 fractures are near-parallel to the BMF and their orientation fits the main foliation plane measured in the micaschists over the slope. The N70 set corresponds to a major regional fracture set evidenced on both sides of the BMF, in the micaschists and amphibolites, and is probably inherited from the regional tectonics (Le Roux et al., 2010). In the accumulation zone, these wide open fractures delineate near vertical slabs locally toppling downhill and have been progressively filled with coarse scree deposits. Finally, the N110–120 fracture set, which is also interpreted as tectonically inherited (Le Roux et al., 2010), is dominant in the depletion zone (Fig. 2). Additional structural data were provided by the north–south oriented exploration gallery (G in Fig. 2a). The gallery description (Vengeon, 1998) shows a succession of pluri-decametric compact blocks separated by meter-to-decameter crushed zones filled with soft clay materials, trending N50 to N70 with 80° northwestward dip. These undeformed blocks are affected by few near-vertical N0 and N90 fractures and by a dense set of N75-oriented short fractures dipping 40–50°S, near-parallel to the slope. These fractures are also visible on the slope surface (Fig. 3) and were recently observed in the first 100 m of a 150 m deep borehole drilled in the accumulation zone (labeled B in Fig. 2a; Bièvre et al., 2012).

The cross-section of Fig. 2c summarizes the main structural features evidenced at the surface and at depth along a survey gallery. At the hectometer to kilometer scale, the main set of fractures, near-vertical and

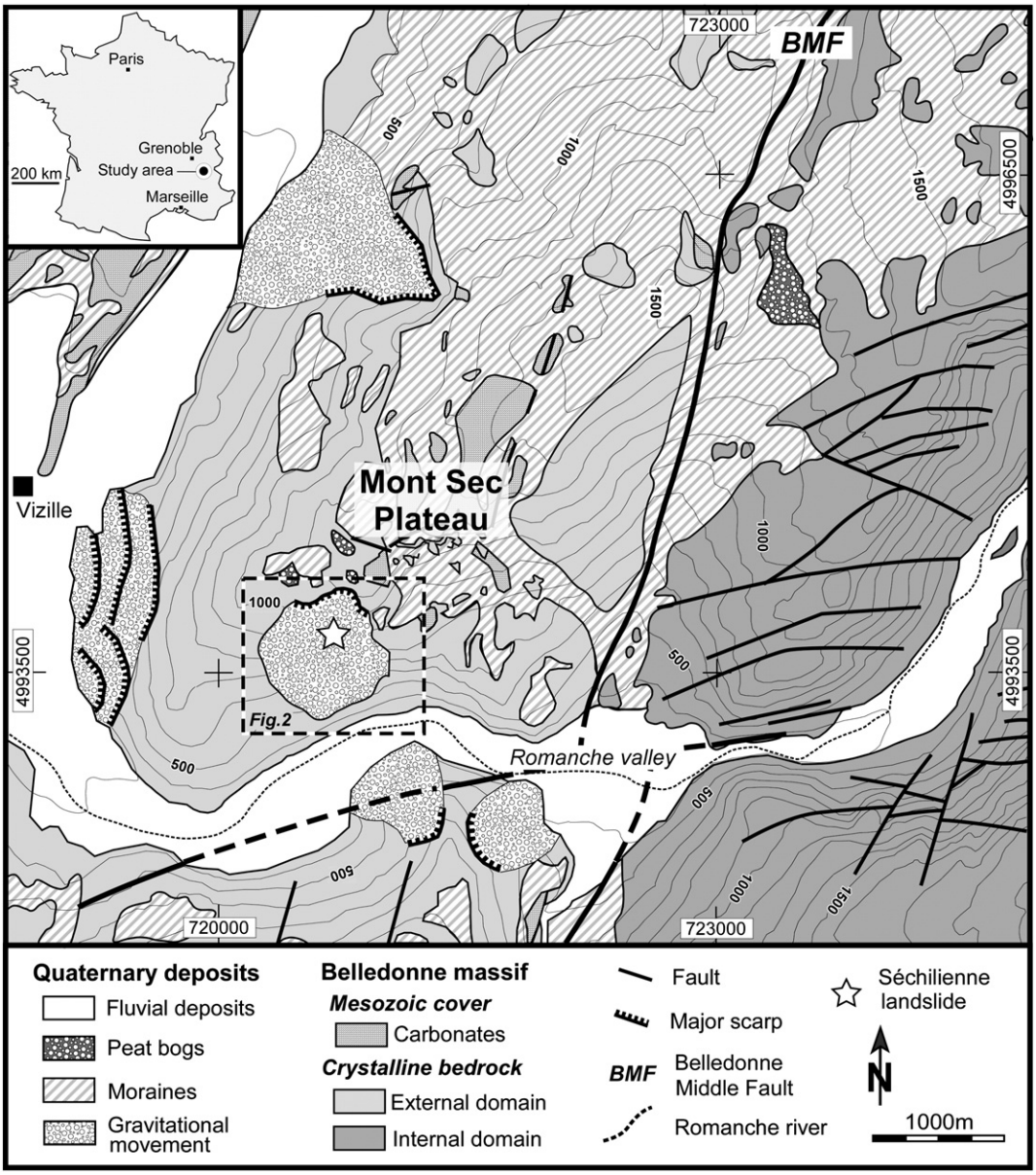

Fig. 1. Geological and structural map of the lower Romanche Valley with the location of the Séchilienne landslide.

trending N70, cuts the whole mass and appears as V-shaped troughs filled with soil deposits at the surface and as crushed zones in the gallery. This major fracture family, which favors the toppling mechanism in the accumulation zone, is cut by numerous pluri-metric fractures dipping near-parallel to the slope. These two sets of fractures result in a stepped geometry that probably controls the downward movement (Fig. 2c). Fracturing parallel to the slope has been commonly observed in sites previously covered by glaciers, and the origin of these fractures has usually been associated with the stress release resulting from deglacial unloading (e.g. Ballantyne and Stone, 2004; Cossart et al., 2008). Eberhardt et al. (2004) documented such fractures in the gneissic slope of the Randa valley where a major rockslide occurred in 1991. Modeling the glacial rebound process at this site, they showed that these tensile fractures parallel to topography could be induced up to a depth of 200 m. However, as mentioned before, the permafrost expansion with time could also have played a role in fracturing the rock mass, preferentially parallel to the slope (Matsuoka and Murton, 2008).

The Séchilienne landslide has been the subject of multiple investigation campaigns for fifteen years (for a recent review, see Le Roux et al., 2011). The combination of the geomorphological and geological analysis, displacement rate values and deep geophysical investigation allowed delineation of the area covered by the landslide (Fig. 2a). The volume affected by the landslide was estimated from deep seismic profiles, bracketed between 48×10^6 m^3 and 63×10^6 m^3 by P-waves velocity (Vp) thresholds at 3000 and 3500 m s^{-1}, respectively (Le Roux et al., 2011). The two landslide limits are shown in the cross-section (Fig. 2c). Cosmic ray exposure (CRE) dating in the area showed that the glacier retreat occurred at 16.6 ± 0.6 ^{10}Be ka at 1120 m a.s.l (Le Roux et al., 2009). By transposing the chronological constraints from the large alpine valley of Tinée (Bigot-Cormier et al., 2005), located 130 km to the South, Le Roux et al. (2009) proposed that the total down-wastage of the Romanche valley at 400 m a.s.l occured at 13.3 ± 0.1 ka. Delunel (2010) calculated a vertical glacier ablation rate between 0.30 and 0.37 m year^{-1} in the valley of Vénéon, filled with a 670 m thick glacier. Applying these ablation rates to the 760 m high Romanche glacier, extending from the bottom of the Romanche valley (380 m) to the Mont Sec plateau (1140 m), provide an age of down-wastage of the valley about 14.3 ± 0.3 ka. Therefore, the failure of the Séchilienne slope head scarp failure initiated at 6.4 ± 1.4 ^{10}Be ka (Le Roux et al., 2009), occurred at least 6200 years after glacial

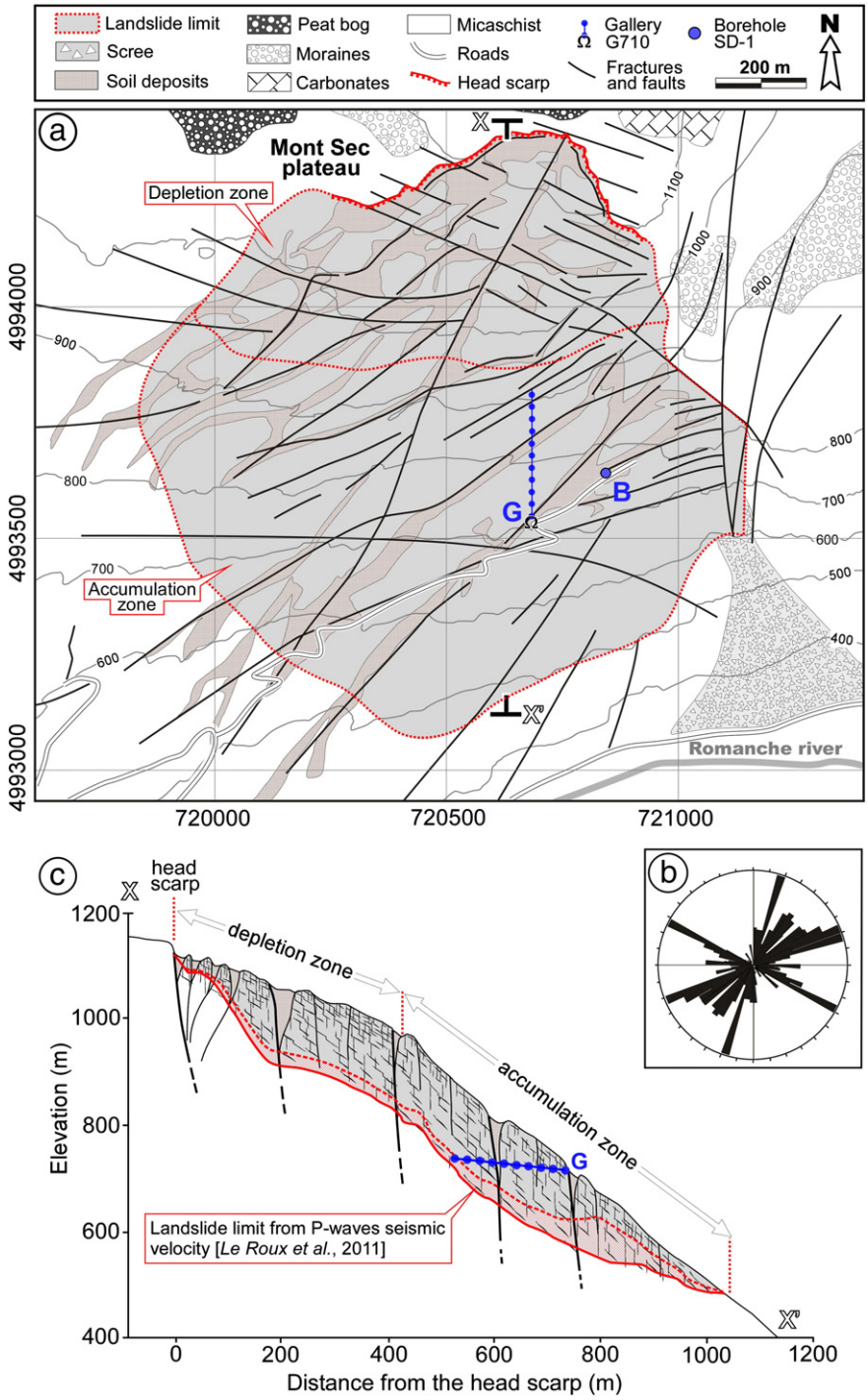

Fig. 2. Geology and geomorphology of the Séchilienne landslide (a) Structural sketch map with the location of the investigation gallery (G) and the borehole (B). (b) Rose diagram of structural data for the Séchilienne slope (modified from Le Roux et al., 2011). (c) North–south cross section with the two main inferred sets of fractures (near-vertical N70 oriented and near-parallel to the slope). The lower seismic limit of the zone affected by the landslide is drawn, considering the two *Vp* threshold limits at 3000 m s^{-1} (dotted red line) and 3500 m s^{-1} (plain red line).

retreat. Therefore the slope destabilization was not an immediate consequence of the Romanche valley debutressing, and the observed delay may have been related to the permafrost persistence at least partly. This hypothesis is examined in the following sections.

3. Ground thermal evolution model

As the climatic and surface conditions prevailing in the study area over the last 21,000 years are poorly known, the simple TTOP model (Smith and Riseborough, 1996) was chosen and coupled with the heat transfer equation in a 2D finite element code for simulating the permafrost temperature variations in the Séchilienne slope. Following Riseborough et al. (2008), the temperature profile is divided in five distinct layers, from top to bottom (Fig. 4): 1) the lower atmosphere, 2) the surface layer (from the base of the lower atmosphere to the Earth surface), 3) the active layer (from the Earth surface to the permafrost table), 4) the permafrost body and 5) the deep ground. The corresponding boundary temperatures are the mean annual air temperature (T_{maa}), the mean annual ground surface temperature (T_{mag}), the mean annual temperature at the top of the permafrost body (T_{top}) and the mean annual

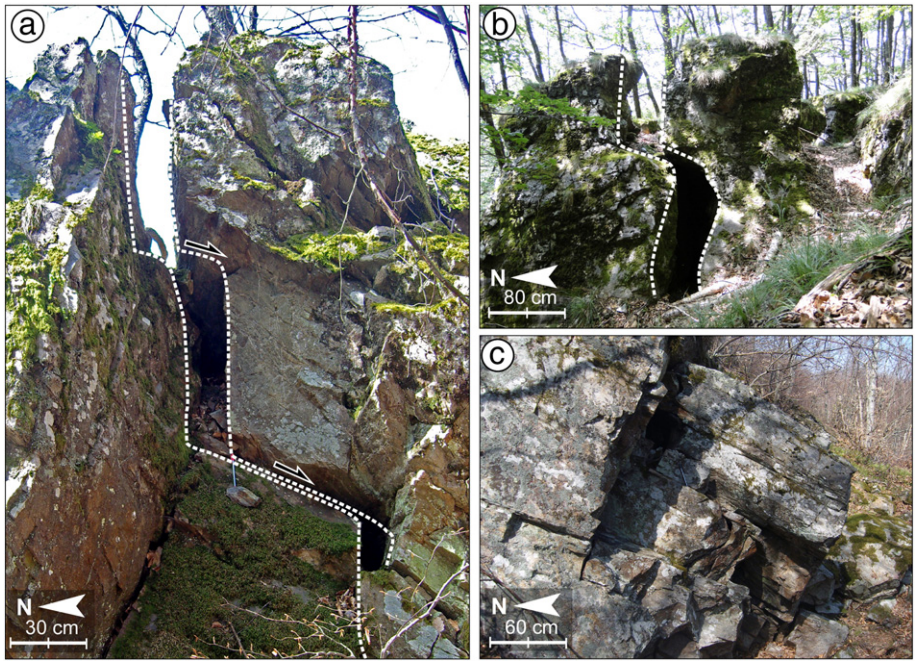

Fig. 3. Photographs of characteristic structures observed in the Séchilienne slope (a) Meter-size fractures dipping nearly parallel to the slope and intersecting the N70 oriented near-vertical fractures. This geometry contributes to the downward motion of the slope. (b) Fracture parallel to the slope in the depletion zone. (c) Penetrative fracture set parallel to the slope in the accumulation zone.

temperature at the bottom of the permafrost body (T_{bot}). The difference between T_{maa} and T_{mag} and that between T_{mag} and T_{top} are called surface offset and thermal offset, respectively (Smith and Riseborough, 1996). The TTOP model combines the processes occurring in the surface layer and in the active layer to estimate the temperature T_{top}. The surface offset (Fig. 4) depends on the isolating and albedo effects of different ground conditions (vegetation, snow cover, forest floor, mineral soils, etc.) and could be estimated by calculation of the surface energy balance. In the TTOP model, these complex processes within the surface layer are simplified and accounted for by the freezing and thawing factors (n_F and n_T, respectively). The n_T factor incorporates all microclimatic effects (radiation, convection, evapotranspiration, etc.) due to vegetation, while n_F is mainly controlled by the influence of snow cover (Smith and Riseborough, 1996). The TTOP model is detailed in Appendix 1.

In and below the permafrost, a simple heat transfer model (Williams and Smith, 1989) is used to relate T_{top} to T_{bot}, considering the geothermal flux and the latent heat phase changes. Fluctuation of permafrost thickness, however, changes the thermal regime by consuming or releasing large amounts of latent heat during freeze/thaw processes, respectively. Following Mottaghy and Rath (2006), the latent heat phase change is accounted for by introducing an effective heat capacity c_e in the heat transfer equation (see Appendix 2).

4. Air temperature reconstruction

The thermal response simulation of the Séchilienne slope requires the mean annual air temperature curve (T_{maa}), from the Late Glacial Maximum (21 ka, Clark et al., 2009) to the present day, as well as the seasonal temperature fluctuations (*ATA*) that are deduced from the mean annual temperatures of the coldest and warmest months (T_{mco} and T_{mwa}, respectively). The three T_{maa}, T_{mco} and T_{mwa} curves over the time period of 21 to 0 ka were reconstructed for the Séchilienne site by compiling curves of several origins and spanning different time intervals (Fig. 5). The following data were considered: (1) recent temporal climatic series characterizing the studied area from 1960 to the present (l'Association Infoclimat, 2011); (2) the Greenland ice core records providing the T_{maa} curve evolution from 40 to 0 ka (Alley, 2000); (3) quantitative pollen climate reconstructions for Central Western Europe giving thermal anomalies of T_{maa}, T_{mco}, and T_{mwa} with respect to the present-day temperature since 12.0 ka (Davis et al., 2003); and (4) T_{mwa} deduced from chironomids and pollen data from 14.0 to 10.8 ka (Ilyashuk et al., 2009). For the present period, the temperature series measured at the Grenoble Saint

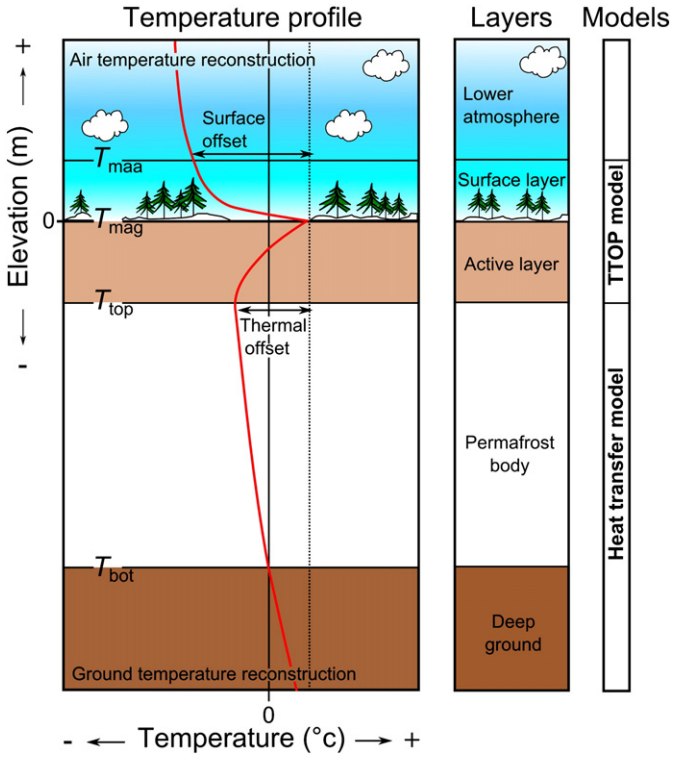

Fig. 4. Permafrost model showing five distinct layers and the temperature vertical profile curve (red line) (modified from Riseborough et al., 2008). T_{bot}: mean annual temperature at the bottom of the permafrost. T_{top}: mean annual temperature at the top of the permafrost. T_{maa}: mean annual air temperature. T_{mag}: mean annual ground surface temperature.

Geoirs meteorological station between 1960 and 2010 was used to produce the T_{maa}, T_{mwa} and T_{mco} curves. This station, located 50 km NW of the Séchilienne slope at an elevation of 384 m a.s.l, required a lapse rate correction to account for the elevation difference to the top of the Séchilienne slope (1140 m a.s.l). Thus, we applied the altitudinal temperature decrease of 5.7 °C km^{-1} proposed by Ortu et al. (2008). The obtained temperatures were taken as present day reference values at 1140 m a.s.l. The temperature variations determined for Central Western Europe between 10.8 to 0 ka (Davis et al., 2003) were applied to compute the T_{maa}, T_{mco}, and T_{mwa} temperature curves at the top of the Séchilienne slope (1140 m a.s.l) during the same period (Fig. 5). The T_{maa} curve was extended to 21 ka by using the Greenland ice core records (Alley, 2000), while the T_{mwa} curve was constrained from 10.8 to 14.0 ka by using chironomids (Ilyashuk et al., 2009). Determining *ATA* from the T_{mwa} and T_{maa} curves allowed the T_{mco} curve to be computed during the same period of time (Fig. 5). Finally, the only missing data (T_{mco} and T_{mwa} curves between 21 and 14 ka) were estimated by assuming a linear relationship between T_{maa} and *ATA* values. These composite temperature curves (T_{mwa}, T_{mco}, and T_{maa}) were used as input data in the thermal modeling of the Séchilienne slope from 21 to 0 ka. Despite a substantial uncertainty, they provide a plausible estimate of the temperature variation at the study site In Fig. 5, four thermal periods were distinguished (labeled A to D) from the temperature curve fluctuations: a cold period A from 21 ka (Last Glacial Maximum) to 14.7 ka with a mean T_{maa} around −8 °C; a warmer period B from 14.7 to 13.0 ka with a T_{maa} between −4.0 °C and +5.5 °C; a short colder period C until 11.6 ka with a mean T_{maa} around −10 °C; and a warmer period D from 11.6 to 0 ka (Holocene) with a T_{maa} between +1.5 °C to +7.5 °C.

5. Numerical model definition

5.1. Thermal scenarios

Because of various interpretations of thermal and surface conditions prevailing in the Séchilienne region over the last 21,000 years, four models were defined, implying two glacier thermal regimes and two ground thermal sets of parameters. First, as glaciers are often polythermal (Owen et al., 2009), two glacier thermal regimes were considered: a cold glacier (regime C) and a temperate glacier (regime T), with a base temperature equal to T_{top} and 0 °C, respectively. Second, thermal ground parameters were usually set constant in numerical modeling (e.g. Kukkonen and Safanda, 2001), although the vegetation and snow cover conditions controlling the *n*-factors significantly varied during the succession of different thermal periods (Fig. 5). Two ground condition scenarios were then considered. In the first one, the *n*-factors were kept constant with time, and the ranges of values ($0.40 \le n_T \le 1.30$; $0.20 \le n_F \le 1.00$) were derived from Lunardini (1978), Jorgenson and Kreig (1988) and Juliussen and Humlum (2007), with the same default values ($n_T = 0.70$ and $n_F = 0.50$) as those used by Smith and Riseborough (1996). In the second scenario, the *n*-factors were defined for each of the four thermal periods (Table 1). During the cold periods A and C (Fig. 5), the n_F factor was computed using the relation proposed by Riseborough and Smith (1998), assuming a snow cover between 0.2 and 1.0 m and an average T_{maa} value of −8 °C and −10 °C for periods A and C, respectively. The corresponding n_T factor values were derived from Juliussen and Humlum (2007) for barren ground surfaces. Under warm periods, both n_F and n_T are controlled by vegetation and the default values and ranges were defined from Lunardini (1978), Jorgenson and Kreig (1988) and Juliussen and Humlum (2007). Finally, glacier-covered areas were characterized by $n_F = 1$ and the n_T values for cold periods (Table 1).

Considering the two glacier thermal regimes (T and C) and the two thermal ground conditions (1 and 2, with constant and time-variable *n*-factors, respectively), we numerically simulated four models (labeled 1C, 1 T, 2C and 2 T). The initial conditions prevailing at 21.0 ka were a surface temperature $T_{maa} = -10$ °C (Fig. 5) and a glacier level at 1200 m a.s.l (Montjuvent and Winistörfer, 1980). Exploiting the CRE data of Le Roux et al. (2009) and Delunel (2010), glacier ablation rates of 0.014 and 0.335 m yr^{-1} were applied before and after 16.6 ka, respectively.

5.2. Methods and the geometrical model

The 2D thermal evolution in the Séchilienne slope was numerically simulated during the last 21,000 years, by implementing the permafrost model of Fig. 4 in the 2D finite-element Comsol software (http://www.

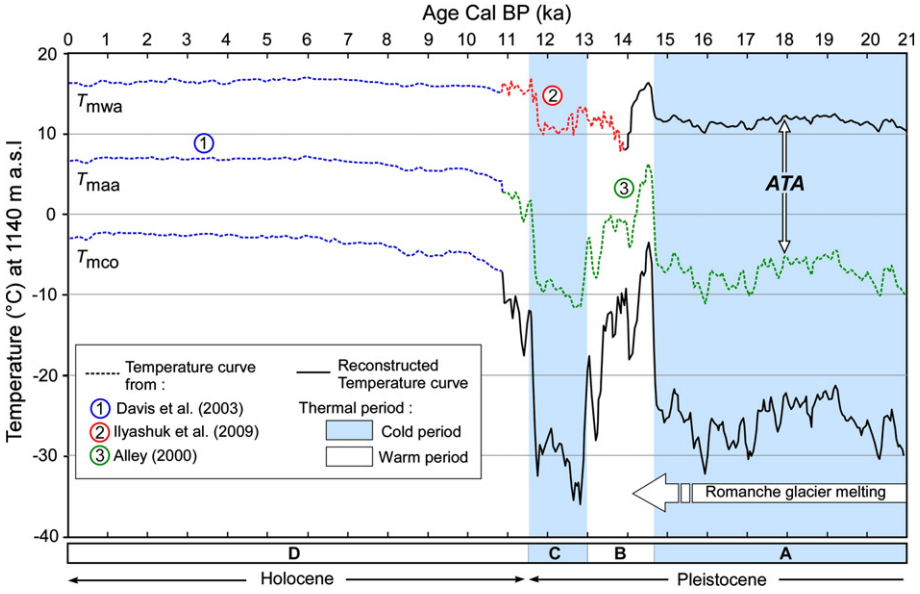

Fig. 5. Paleo-temperature curves from the last 21,000 years (see text for details). Temperature data are in dotted lines, with different colors according to the authors: (1) blue: Davis et al. (2003); (2) red Ilyashuk et al. (2009); and (3) green: Alley (2000). Chronologies of Davis et al. (2003) and Ilyashuk et al. (2009) are based on ^{14}C calibrated ages, whereas that of Alley (2000) is based on the GISP2 ice core. Both our data and the reference data are plotted on the Cal BP scale. Reconstructed temperatures are in solid lines. T_{mwa}: mean annual temperature curve for the warmest months. T_{maa}: mean annual air temperature curve. T_{mco}: mean annual temperature curve for the coldest months. *ATA*: annual temperature amplitude. Four climate periods (labeled A to D) are distinguished. The melting of the Romanche glacier in the valley bottom until 14.3 ka is also indicated.

comsol.com). First, the slope geometry before destabilization was approximately reconstructed along the N–S cross-section of Fig. 2c by balancing the depletion and accumulation surfaces (Fig. 6). It resulted in a simple 40° slope cut by the Mont Sec plateau and the valley at 1140 and 380 m a.s.l., respectively. This model was laterally and vertically extended to reduce the boundary effects and was gridded (Fig. 7), using a mesh composed of 1758 triangular elements with a size between 65 and 135 m. The temperature evolution in the slope over the last 21,000 years was simulated with a time step of 4.2 years. A null horizontal heat flux was applied at both vertical boundaries of the model, while a constant vertical upward heat flow of 65 mW m^{-2}, similar to the present-day flux (Lucazeau and Vasseur, 1989; Goy et al., 1996), was imposed at the bottom of the model.

5.3. Parameters

The model was supposed homogeneous and the parameter values used for the thermal simulation are given in Table 2 (default values and ranges of variation). Porosity and bulk density values (ϕ and ρ_d) were determined by previous laboratory tests performed on micaschist samples (Le Roux et al., 2011), with default values of 3.7% and 2730 kg m^{-3}, respectively. Porosity was bracketed between 0.9% and 5.3%. Although micaschists are thermally anisotropic, a unique thermal conductivity value k_T of 2.5 W m^{-1} °C^{-1} was considered in thawed rock (Goy et al., 1996), while a specific heat capacity value of $c = 800$ J kg^{-1} °C^{-1} was taken from the literature (Stacey and Davis, 2008). A ground conductivity ratio $r_k = k_T/k_F$ between 0.25 and 1 was considered, with a default value fixed at 0.5 (Smith and Riseborough, 1996). A freezing interval parameter θ of 0.3 °C was taken between the solidus and liquidus temperatures (Wegmann et al., 1998). Finally, as ground temperatures also depend on the solar radiation (Blackwell et al., 1980), which is controlled by the slope angle and orientation, we also considered a scenario with a temperature correction of +0.4 °C applied to the south-facing 40° Séchilienne slope (Safanda, 1999; Table 1). The T_{top} values at the ground surface were calculated from the air temperature curves of Fig. 5, using Eq. (1) in Appendix 1. A thermal gradient of 5.7 °C km^{-1} was considered for elevation corrections (Ortu et al., 2008).

6. Modeling results

The temperature evolution in the slope was simulated for the four models, considering the default values shown in Table 2. The temperature distributions computed for Model 1 T (constant *n*-factors and temperate glacier) at seven different times (Fig. 8b) are plotted with an interval of 2 °C (Fig. 8a), along with the extension of the permafrost (dark blue) and the glacier (light blue). Permafrost depths measured perpendicular to the slope at four points (P1 to P4, Fig. 8a) are given in Table 3 for five different times with an accuracy of ±10 m. Notably, the permafrost limits are roughly parallel to the slope surface. At 21.0 ka (time 1 in Fig. 8b), there was no permafrost since the long-term temperature at the bottom of the temperate glacier was zero. During the cold period A (times 2 and 3, 16.6 and 15.0 ka), the permafrost gradually spread into the upper and middle parts of the ice-free slope, following the glacier lowering. The maximum permafrost thickness reached about 190 m (Table 3). During the warmer period B (time 4, 14.1 ka), the permafrost thinned and

Table 1
Default values and variation ranges of the *n*-factors used in the scenario 2 for the four thermal periods (A to D) and ground surfaces covered by the glacier.

n-factors		Thermal period				Glacier
		D	C	B	A	
n_F	Range of values	0.25–0.35	0.30–0.70	0.25–0.35	0.20–0.60	–
	Default values	0.30	0.50	0.30	0.40	1.00
n_T	Range of values	0.40–0.80	0.90–1.30	0.40–0.80	0.90–1.30	0.90–1.30
	Default values	0.60	1.10	0.60	1.10	1.10

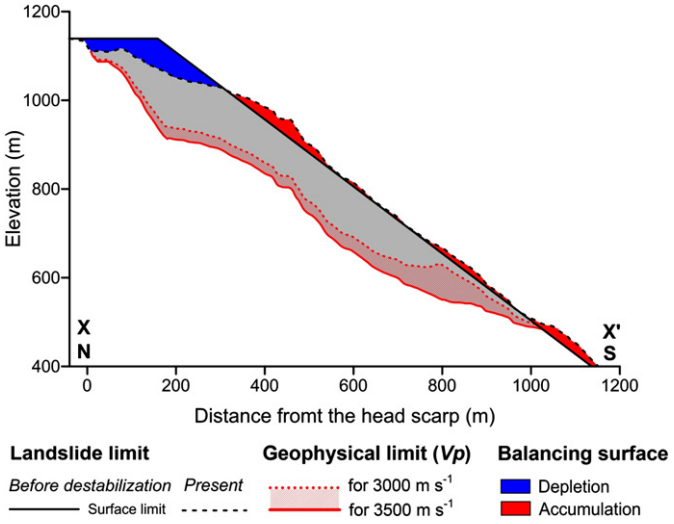

Fig. 6. 2D reconstruction of the Séchilienne slope geometry before destabilization corresponding to the cross-section in Fig. 2c, obtained by balancing the depletion and accumulation surfaces. The uncertainty on the landslide base (threshold between 3000 and 3500 m s^{-1}) is shown with red lines.

just an iced core remained in the upper part of the slope. During the following cooler period C (times 5 and 6, 13.0 and 12.0 ka), the permafrost developed into the slope to reach again a maximum depth of 190 m. At the beginning of the Holocene (period D, time 7, 10.0 ka), the temperature rose quickly before stabilizing, provoking the quick melt of the permafrost that vanished.

Simulations for the other three models 1C, 2C and 2 T are shown in Fig. 9 at the same periods/times, and corresponding permafrost depths are given in Table 3. Under cold glacier conditions, the slope was initially frozen to a depth varying between 150 and 350 m for model 1C and 100 and 225 m for model 2C (Fig. 9). During the cold period A (21.0 to 15.0 ka), the glacier progressively lowered and the permafrost volume

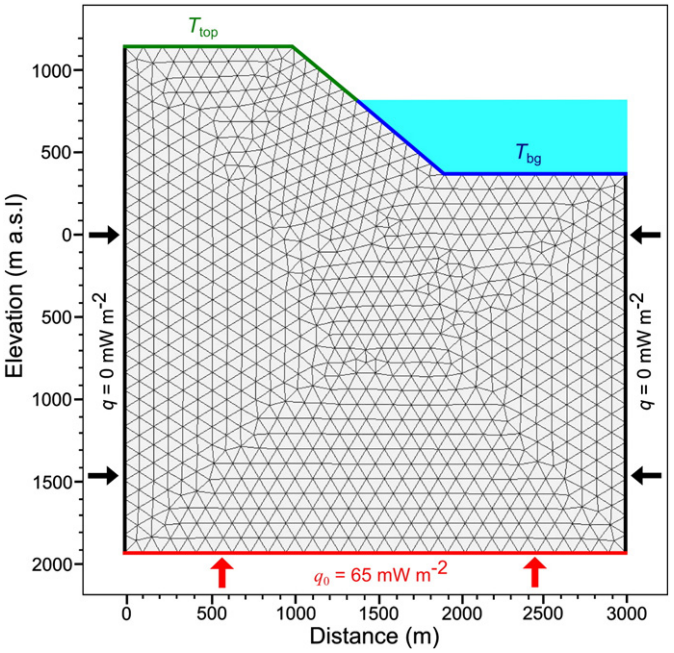

Fig. 7. 2D Séchilienne slope model with the applied boundary conditions. The glacier at 15.6 ka is in blue. T_{top}: Temperature deduced from the TTOP model and imposed at the surface. T_{bg}: Temperature at the base of the glacier. The thickness of the glacier varies between 0 and 820 m.

Table 2
Default values and variation ranges for the parameters used in the model. See text for details.

	Model parameters	Range of values	Default values	Units
ϕ	Porosity	0.9–5.3	3.7	%
ρ_d	Dry bulk density	—	2730	kg m^{-3}
c	Specific heat capacity	—	800	J kg^{-1}
k_T	Thermal conductivity	—	2.5	W m^{-1}
r_k	Ground conductivity ratio (k_T/k_F)	0.25–1.00	0.5	—
θ	Freezing interval	—	0.3	—
n_f	Freezing *n*-factor	0.20–1.00	0.5	—
n_T	Thawing *n*-factor	0.4–1.3	0.7	—
s_c	Slope attitude correction	0.0–0.4	0.0	—
q_0	Geothermal flux	—	65	mW m^{-2}

slightly decreased to reach a thickness ranging from 95 to 315 m for model 1C and 45 to 165 m for model 2C. During the warmer period B (14.1 ka), the glacier disappeared from the valley and the permafrost was reduced to a thick core in the upper part of the slope, with a much larger extension for model 1C. At 13.0 ka, the cold thermal period C initiated a new growing of the permafrost along the slope, which reached a depth between 120 and 255 m (Model 1C) and from 70 to 170 m (Model 2C) at 12.0 ka. The permafrost disappeared at 10.3 ka for Model 1C and about 1000 years earlier for Model 2C.

Finally, the permafrost evolution with time for Model 2 T (variable *n*-factors in Table 1) is similar to that described for Model 1 T (Fig. 8), with lower permafrost depths. In Table 3, permafrost depths at P1 to P4 for the four models are compared at the five different times along with the permafrost disappearance age. A striking feature is that the permafrost totally melts in the same time range (11.0 to 10.0 ka)

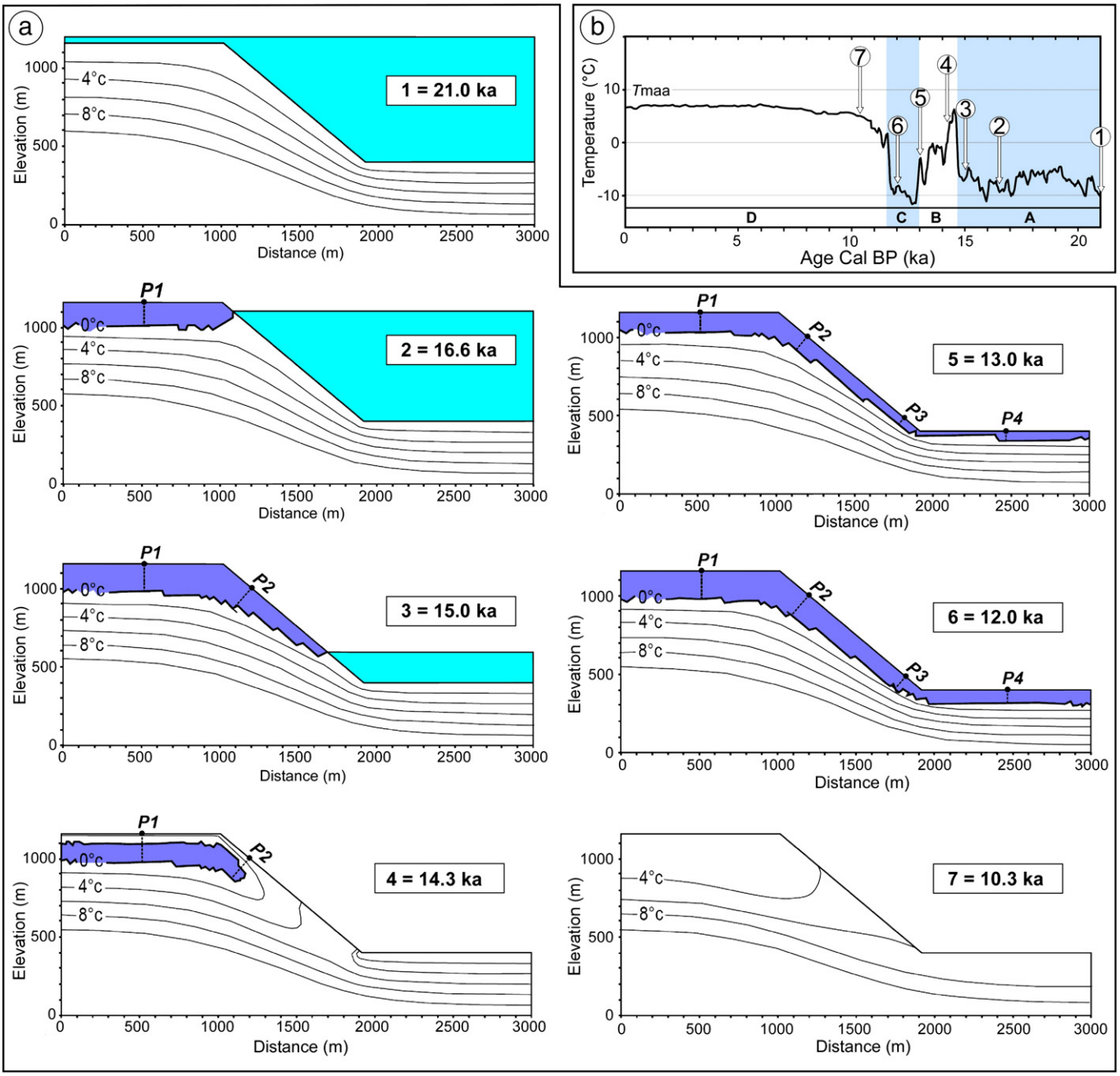

Fig. 8. Results of 2D thermal numerical modeling (a) Temperature distributions simulated for model 1 T (constant *n*-factors $n_T = 0.7$ and $n_F = 0.5$ and temperate glacier) at the seven different times shown in (b). The permafrost and glacier extensions are shown in dark and light blue, respectively. P1 to P4 show the locations where permafrost thickness values were extracted (Table 3).

Table 3
Depth of the permafrost base (in m) at four sites (P1 to P4) shown in Fig. 8. The maximum permafrost depth reached at each site is indicated in bold for the four models. In the last column, the age of the permafrost disappearance is given for each model.

Model	t = 16.6 ka				*t* = 15.0 ka				*t* = 14.3 ka				*t* = 13.0 ka				*t* = 12.0 ka				Permafrost disappearance
	Permafrost depth (m)				Permafrost depth (m)				Permafrost depth (m)				Permafrost depth (m)				Permafrost depth (m)				
	P1	P2	P3	P4	P1	P2	P3	P4	P1	P2	P3	P4	P1	P2	P3	P4	P1	P2	P3	P4	age (ka)
Model 1 T	160	—	—	—	**195**	175	—	—	195	180	—	—	135	130	70	75	190	**190**	**115**	**105**	10.5
Model 1C	**315**	**330**	**125**	**130**	315	305	125	95	300	305	—	—	220	185	65	70	255	245	120	125	10.2
Model 2C	**170**	180	**70**	**70**	165	**185**	65	65	170	180	—	—	100	100	—	—	170	155	65	70	10.9
Model 2 T	**135**	—	—	—	130	125	—	—	—	—	—	—	105	95	—	—	130	**130**	**70**	**75**	11.1

for all simulations. The comparison of the permafrost depths along the slope shows that the maximum extension of permafrost (330 m at the top of the slope) was obtained for Model 1C, while the more limited extension was observed for Model 2 T (125 m at the same site). For the same glacier conditions, accounting for time-dependent *n*-factors resulted in less development of the permafrost than the extension computed with constant *n*-factors. Notably, for cold glacier conditions (Models 1C and 2C), the maximum permafrost depths were reached during the first cold period A, while they were observed during the second cold period (C) under temperate glacier conditions.

7. Discussion

The maximum depth reached by the permafrost along the slope is plotted in Fig. 10 for the four models. Three models (1 T, 2 T and 2C) yield relatively similar results, while a significant deviation in permafrost depth (330 m) is observed for Model 1C. Although cold glacier conditions cannot be locally excluded, the strong glacial erosion observed in the Western Alps (Owen et al., 2009) is in favor of a temperate regime at Séchilienne. In particular, Model 1C (constant *n*-factors and cold glacier) is the least plausible among the considered models and can be discarded. The permafrost penetration obtained for Model 1 T (105 to 195 m) is compared to the thickness values (100 to 250 m) computed by Kukkonen and Safanda (2001) in northern Fennoscandia, using the TTOP model under the same conditions. In both studies, depth values are of the same order of magnitude. As concluded by Kukkonen and Safanda (2001), depth estimations could be improved by accounting for the changes in snow and vegetation cover. In order to define the most impacting parameter on the modeling results, we performed a sensitivity analysis for models 1C and 1 T, varying the five poorly constrained parameters (, r_k, n_T, n_F and s_c) in the range indicated in Table 2. The results (not shown) indicate that the predominant parameter is n_F, underlining again the need to better precise the *n*-factor values for modeling. The effect of *n*-factor fluctuations with climate was investigated in Model 2 T and it turned out that the permafrost penetration was about 30% less in this case (70–135 m; Table 3 and Fig. 10). Sensitivity tests were made for the same Model 2 T, focusing on the *n*-factor variations in the range shown in Table 2. The maximum observed effect is a permafrost persistence variation of 600 years and a depth fluctuation of 30 m with respect to the default values.

The maximum depth reached by the permafrost for the three models (1 T, 2 T and 2C) is comparable to the depth affected by the landslide along the same cross-section (Fig. 10), considering the two *Vp* threshold limits (3000 and 3500 m s^{-1}) proposed by Le Roux et al. (2011). The maximum permafrost depths computed along the slope are of the same order of magnitude (100 to 190 m) as the thickness of the damaged zone imaged by the seismic investigation (Le Roux et al., 2011). This comparison suggests that the long-term permafrost front fluctuations during the last 21,000 years could have played a role in mechanically degrading the slope through ice segregation, a mechanism suggested by Wegmann et al. (1998) and Kukkonen and Safanda (2001) in other regions. This hypothesis is supported by the observation of meter-size fractures nearly parallel to the slope, both at the surface and in the first 100 m of borehole B. The common explanation for this fracture pattern is the stress release following deglacial unloading (Ballantyne and Stone, 2004; Cossart et al., 2008). The penetration and intensity of fracturing during debutressing strongly depend on rock mechanical characteristics (Augustinus, 1995), which then could have been controlled by the permafrost-induced slope weakening.

Our results are synthesized in Fig. 11, which shows the chronological constraints on the events that could have affected the Séchilienne slope. From CRE dating, the final total down-wastage of the Romanche valley was estimated at 14 ka (Tg^r), at least 6200 years before the initiation of Séchilienne head scarp. This delay can be considered as a minimal pre-failure endurance corresponding to the time interval following the disappearance of the glacier during which the slope endures the new state of stress before the initiation of failure. Thermal modeling results suggest that permafrost vanished in the Séchilienne slope between 10 and 11 ka (Tp), i.e. at least 2000 to 3000 years before the Séchilienne head scarp failure. These results suggest that the permafrost disappearance did not directly cause the failure but its persistence could have delayed the rupture by a few thousand years, by mechanically strengthening the slope. Finally, the head scarp destabilization occurred at 6.4 ka (Td^i), during the warmer and wetter Climatic Optimum period (Davis et al., 2003; Magny, 2004). This suggests that increases in temperature and precipitation during the Middle Holocene significantly contributed to the Séchilienne slope destabilization. Fig. 11 emphasizes that the permafrost expansion and degradation since 21,000 years played a key role in the Séchilienne slope development, in a multiprocess phenomenon including glacial debutressing and the Pleistocene to Holocene climate change.

8. Conclusions

The thermal numerical modeling of the Séchilienne slope during the last 21,000 years showed that permafrost vanished around 10 to 11 ka and therefore persisted at least 3000 to 4000 years after total ice down-wastage in the Romanche valley. The strengthening effect of ice can only partly explain the 6200-year delay measured between glacial retreat and instability initiation of the head scarp, which occurred during the wet and warm Climatic Optimum period. These results support the interpretation of a predominant role of climate on slope destabilization, although the effect of seismic activity cannot be ruled out completely. This study also reveals that, under the most plausible conditions (temperate glacier and time-dependent *n*-factors), the permafrost below the Séchilienne slope since the Last Glacial Maximum (LGM) reached a maximum thickness of 70 to 135 m, which corresponds to the destabilization depth inferred from seismic prospecting. These observations suggest that permafrost expansion weakened the Séchilienne slope and controlled the thickness of ground fractured after glacial unloading.

Permafrost development and longevity have turned out to be factors controlling slope stability, in addition to those usually proposed such as glacial debutressing, climate changes and active tectonics. In particular, deep permafrost expansion is shown to play a significant role in the development of deep-seated landslides in previously glaciated areas. The effect of permafrost is, however, hard to know from direct field observations, and its importance in comparison with that of the other factors is still difficult to assess. Understanding complex gravitational

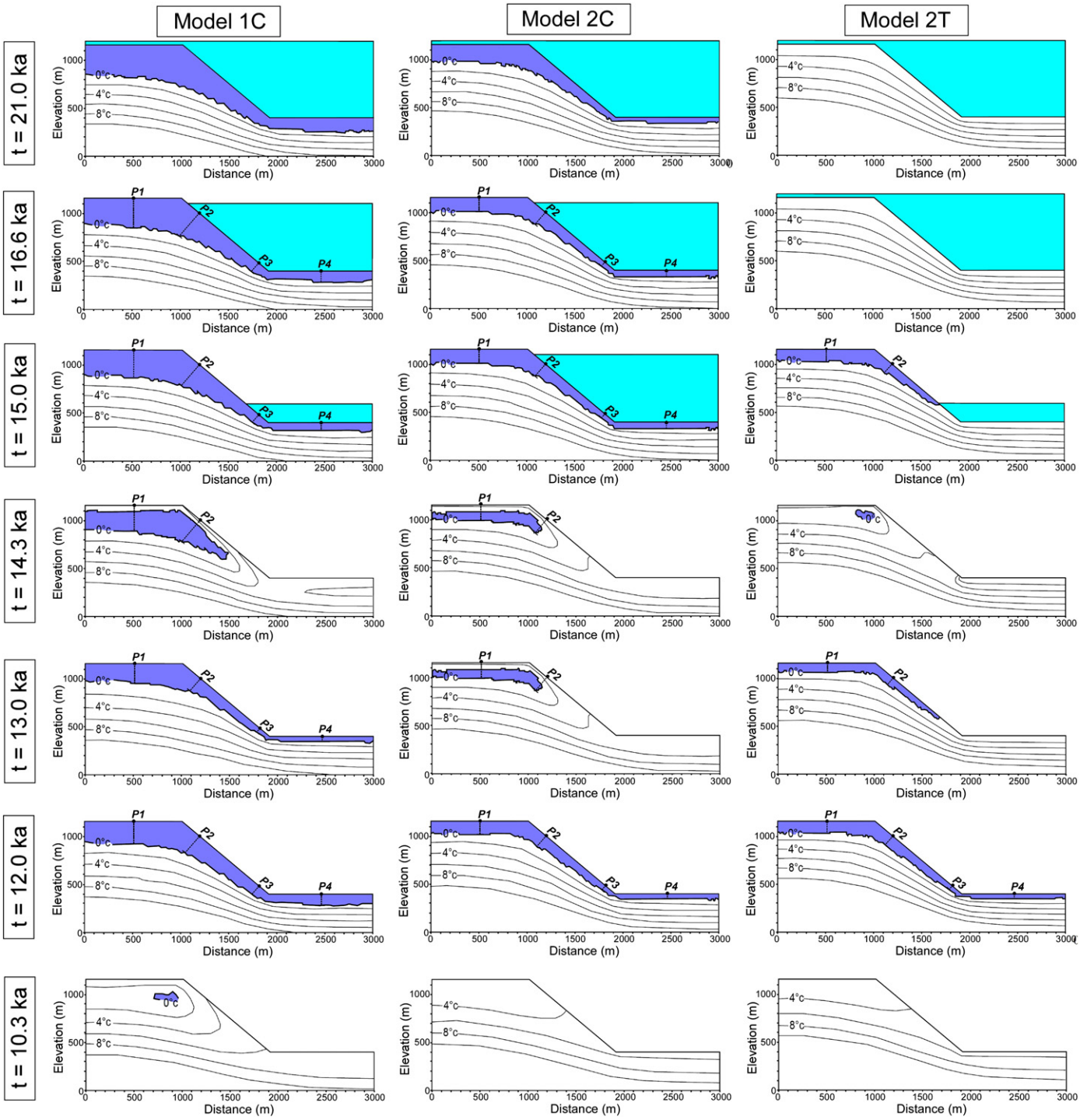

Fig. 9. 2D temperature distributions simulated for the three models 1C, 2C and 2 T (1: constant *n*-factors; 2: variable *n*-factors; C: cold glacier; T: temperate glacier) at different times, applying the temperature curves in Fig. 5. The permafrost and glacier extensions are shown with deep and light blue colors, respectively. P1 to P4 show the locations where permafrost thickness values were extracted (Table 3).

movements requires further investigation combining CRE dating and thermo-mechanical finite element modeling.

Acknowledgements

This study was supported by the Agence Nationale de la Recherche project “ANR-09-RISK-008”. We would like to thank Jérôme Nomade for fruitful discussion on climatic curve reconstruction and William Mahaney for the improvement of the manuscript. We also thank the two anonymous reviewers and Takashi Oguchi for their critical reviews.

Appendix 1

In the TTOP model the n_T and n_F factors are applied as transfer functions between T_{maa} and T_{mag}. In the active layer, the thermal offset, which results from the difference in thermal conductivity values

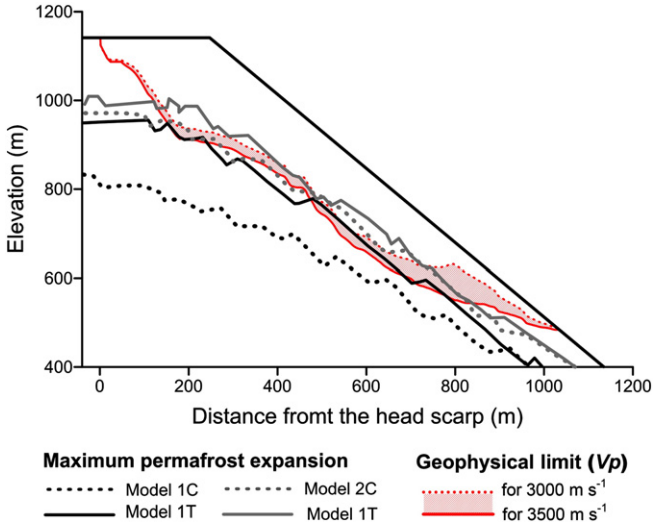

Fig. 10. Maximum permafrost depths computed for the four models (default values) along the Séchilienne slope before destabilization. They are compared with the landslide geometry, considering the two thresholds at 3000 m s^{-1} (dotted red line) and 3500 m s^{-1} (solid red line).

between frozen and thawed grounds, is related to ground thermal properties and to the ground surface temperature. The effects of active and surface layers are combined to obtain the following equation (Smith and Riseborough, 1996):

$$T_{top} = \frac{k_T n_T I_{TA} - k_F n_F I_{FA}}{Pk^*} \quad \text{with} \quad k^* = \left\{ \begin{array}{l} k_F \text{ if } k_T I_{TS} - k_F I_{FS} < 0 \\ k_T \text{ if } k_T I_{TS} - k_F I_{FS} > 0 \end{array} \right\} \quad (1)$$

where k_F and k_T are the thermal conductivity values for the frozen and thawed ground, n_F and n_T are the freezing and thawing factors, I_{FA} and I_{TA} are the air seasonal freezing and thawing degree-day indexes, I_{FS} and I_{TS} surface seasonal freezing and thawing-degree days indexes, and P is the period (365 days) of temperature fluctuations. Air seasonal indexes can be deduced from the mean annual air temperature curve and the annual temperature amplitude (Smith and Riseborough, 1996).

Appendix 2

The effective heat capacity c_e is introduced in the heat transfer equation:

$$-div \ \vec{q} = \rho c_e \dot{T} \quad with \quad c_e = c + \frac{L}{1 + \left(\frac{1}{2} - 1\right)\frac{\rho_d}{\rho_w}} f \quad (2)$$

where $\vec{q}$ is the conductive heat flux density, ρ is the total rock density, T is the temperature, c is the specific heat capacity of rock at constant pressure, L ($=3.35 \times 10^5$ J kg^{-1}) is the latent heat of fusion for water, ρ_w ($=1000$ kg m^{-3}) is the density of water, ρ_d is the dry bulk density and f is the frozen content of water.f is given by the following equation:

$$f = H(T_T - T).\frac{2T}{\theta^2} e^{-\left(\frac{T_T + T}{\theta}\right)^2} \quad (3)$$

where H is the Heaviside function, T_T is the melting point and θ is the freezing interval.

References

Alley, R.B., 2000. GISP2 ice core temperature and accumulation data. IGBP PAGES/World Data Center for Paleoclimatology. : Data Contribution Series No. 2004–013NOAA/NGDC Paleoclimatology Program, Boulder CO, USA.

Augustinus, P.C., 1995. Glacial valley cross-profile development: the influence of in situ rock stress and rock mass strength, with examples from the southern Alps, New Zealand. Geomorphology 14, 87–97.

Ballantyne, C.K., 2002. Paraglacial geomorphology. Quaternary Science Reviews 21, 1935–2017.

Ballantyne, C.K., Stone, J.O., 2004. The Beinn Alligin rock avalanche, NW Scotland: cosmogenic ^{10}Be dating, interpretation and significance. The Holocene 14, 448–453.

Bièvre, G., Kasperski, J., Pothérat, P., 2012. Séchilienne — Programme de reconnaissances. Interprétation géologique des sondages. : Technical Report CETE de Lyon 40320–1 and 41106–1CETE de Lyon, Lyon, France.

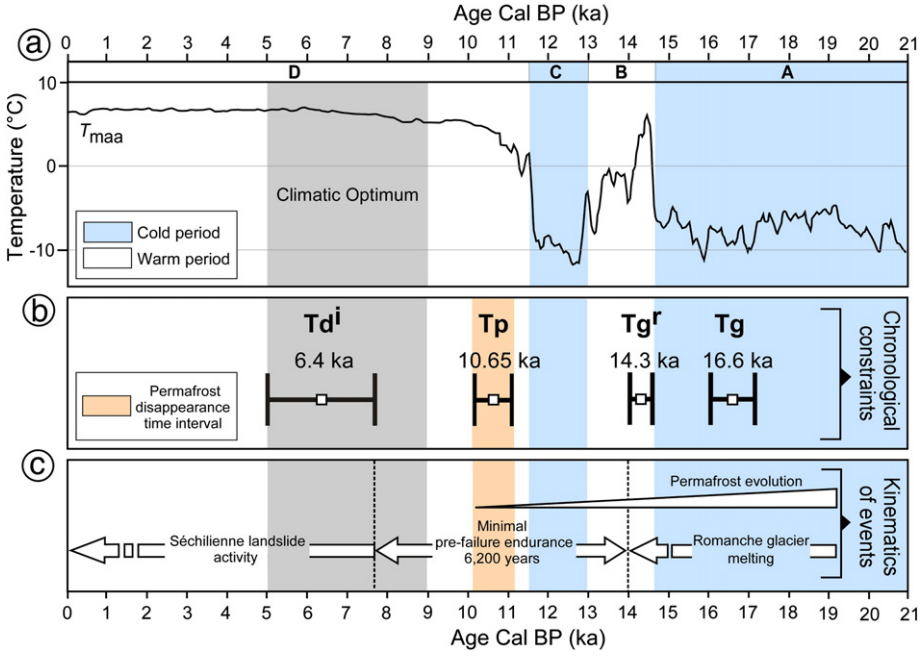

Fig. 11. Succession of kinematics events affecting the Séchilienne slope after the thermal and chronological constraints (a) Mean annual air temperature curve from the Last Glacial Maximum (21 ka) up to the present day in the Séchilienne slope at 1140 m a.s.l, the Holocene Climatic Optimum period is indicated in grey (b) Chronological constraints. Tg: age of the glacier retreat at 1100 m a.s.l (Le Roux et al., 2009); Tg^r: age of the glacier retreat in the valley at 380 m a.s.l.; Tp: age of permafrost disappearance inferred from thermal modeling; and Td^i: initiation phase of the head scarp destabilization (Le Roux et al., 2009) (c) Kinematics of the Séchilienne slope deduced from the chronological data related to glacier melting. Permafrost evolution and landslide activity yielded a minimal pre-failure endurance of 6200 years.

Bigot-Cormier, F., Braucher, R., Bourlès, D., Guglielmi, Y., Dubar, M., Stéphan, J.F., 2005. Chronological constraints on processes leading to large active landslides. Earth and Planetary Science Letters 235, 141–150.
Blackwell, D.D., Steele, J.L., Brott, C.A., 1980. The terrain effect on terrestrial heat flow. Journal of Geophysical Research 85, 4757–4772.
Clark, P.U., Dyke, A.S., Shakum, J.D., Carlson, A.E., Clark, J., Wohlfarth, B., Mitrovica, J.X., Hostetler, S.W., McCabe, A.M., 2009. The last glacial maximum. Science 325, 710–714.
Cossart, E., Braucher, R., Fort, M., Bourlès, D., Carcaillet, J., 2008. Slope instability in relation to glacial debutressing in alpine areas (upper durance catchment, southeastern France): evidence from field data and ^{10}Be cosmic ray exposure ages. Geomorphology 95, 3–26.
Cruden, D.M., Hu, X.Q., 1993. Exhaustion and steady states models for predicting landslides hazards in the Canadian Rocky Mountains. Geomorphology 8, 279–285.
Davis, B., Brewer, S., Stevenson, A., Guiot, J., data contributors, 2003. The temperature of Europe during the Holocene reconstructed from pollen data. Quaternary Science Reviews 22, 1701–1716.
de Beaulieu, J.L., 1977. Contribution pollenanalytique à l'histoire tardiglaciaire et holocène de la végétation des Alpes méridionales françaises. (PhD thesis) Université Aix-Marseille III, Marseille (391 pp.).
Delunel, R., 2010. Evolution géomorphologique du massif des Ecrins-Pelvoux depuis le Dernier Maximum Glaciaire. (PhD thesis) Université Grenoble I, Grenoble (236 pp.).
Delunel, R., van der Beek, P., Carcaillet, J., Bourlès, D., Valla, P., 2010. Frost-cracking control on catchment denudation rates: Insights from in situ produced ^{10}Be concentrations in stream sediments (Ecrins–Pelvoux massif, French Western Alps). Earth and Planetary Science Letters 293, 72–83.
Deplazes, G., Anselmetti, F.S., Hajdas, I., 2007. Lake sediments deposited on the Flims rockslide mass: the key to date the largest mass movement of the Alps. Terra Nova 19, 252–258.
Eberhardt, E., Stead, D., Coggan, J.S., 2004. Numerical analysis of initiation and progressive failure in natural rock slopes — the 1991 Randa rockslide. International Journal of Rock Mechanics and Mining Sciences 41, 69–87.
Goy, L., Fabre, D., Ménard, G., 1996. Modelling of rock temperatures for deep alpine tunnel projects. Rock Mechanics and Rock Engineering 29, 1–18.
Gruber, S., Haeberli, W., 2007. Permafrost in steep bedrock slopes and its temperature related destabilization following climate change. Journal of Geophysical Research 112, F02S18. http://dx.doi.org/10.1029/2006JF000547.
Guglielmin, M., Cannone, N., Dramis, F., 2001. Permafrost–glacial evolution during the Holocene in the Italian Central Alps. Permafrost and Periglacial Processes 12, 111–124.
Guillot, S., Di Paola, S., Ménot, R.P., Ledru, P., Spalla, M.I., Gosso, G., Schwartz, S., 2009. Suture zones and importance of strike-slip faulting for Variscan geodynamic reconstructions of the External Crystalline Massifs of the western Alps. Bulletin de la Societe Geologique de France 180, 483–500.
Hormes, A., Ivy-Ochs, S., Kubik, P.W., Ferreli, L., Michetti, A.M., 2008. ^{10}Be exposure ages of rock avalanche and a late glacial moraine in Alta Valtellina, Italian Alps. Quaternary International 190, 136–145.
Ilyashuk, B., Gobet, E., Heiri, O., Lotter, A.F., van Leeuwen, J.F.N., van der Knaap, W.O., Ilyashuk, E., Oberli, F., Ammann, B., 2009. Lateglacial environmental and climatic changes at the Maloja pass, Central Swiss Alps, as recorded by chironomids and pollen. Quaternary Science Reviews 28, 1340–1353.
Ivy-Ochs, S., Poschinger, A.V., Synal, H.A., Maisch, M., 2009. Surface exposure dating of the Flims landslide, Graubünden, Switzerland. Geomorphology 103, 104–112.
Jorgenson, M.T., Kreig, R.A., 1988. A model for mapping permafrost distribution based on landscape component maps and climatic variables. Fifth International Conference on Permafrost (Trondheim, Norway). : , 1. Tapir Publishers, Trondheim, pp. 176–182.
Juliussen, H., Humlum, O., 2007. Towards a TTOP ground temperature model for mountainous terrain in central- eastern Norway. Permafrost and Periglacial Processes 18, 161–184.
Korup, O., Clague, J.J., Hermanns, R.L., Hewitt, K., Strom, A.L., Weidinger, J.T., 2007. Giant landslides, topography, and erosion. Earth and Planetary Science Letters 261, 578–589.
Krivonogova, N.F., 2009. Characteristics of the composition, structure and physico-mechanical properties of permafrost rock soil in massifs. Soil Mechanics and Foundation Engineering 46, 136–146.
Kukkonen, I.T., Safanda, J., 2001. Numerical modelling of permafrost in bedrock in northern Fennoscandia during the Holocene. Global and Planetary Change 29, 259–273.
l'Association Infoclimat, 2011. Infoclimat web page. http://www.infoclimat.fr.
Le Roux, O., Schwartz, S., Gamond, J.F., Jongmans, D., Bourlès, D., Braucher, R., Mahaney, W., Carcaillet, J., Leanni, L., 2009. CRE dating on the head scarp of a major landslide (Séchilienne, French Alps), age constraints on Holocene kinematics. Earth and Planetary Science Letters 280, 236–245.
Le Roux, O., Schwartz, S., Gamond, J.F., Jongmans, D., Tricart, P., Sébrier, M., 2010. Interaction between tectonic and erosion processes on the morphogenesis of an alpine valley: geological and geophysical investigations in the lower Romanche valley (Belledonne massif, western Alps). International Journal of Earth Sciences 99, 427–441.
Le Roux, O., Jongmans, D., Kaperski, J., Schwartz, S., Potherat, P., Lebrouc, V., Lagabrielle, R., Meric, O., 2011. Deep geophysical investigation of the large Séchilienne landslide (western Alps, France) and calibration with geological data. Engineering Geology 120, 18–31.
Lucazeau, F., Vasseur, G., 1989. Heat flow density data from France and surrounding margins. Tectonophysics 164, 251–258.
Lunardini, V.J., 1978. Theory of n-factors and correlation of data. Paper presented at 3rd International Conference on Permafrost. International Permafrost Association, Edmonton, Canada.
Magny, M., 2004. Holocene climate variability as reflected by mid-European lake-level fluctuations and its probable impact on prehistoric human settlements. Quaternary International 113, 65–79.
Magny, M., 2007. Climate oscillations and hydrological variations in Europe over the last 15,000 years. Lettre pigb-pmrc-France 20, 72–76.
Matsuoka, N., Murton, J., 2008. Frost weathering: recent advances and future directions. Permafrost and Periglacial Processes 19, 195–210.
Matsuoka, N., Hirakawa, K., Watanabe, T., Haeberli, W., Keller, F., 1998. The role of diurnal, annual and millennial freeze-thaw cycles in controlling alpine slope stability, paper presented at 7th International Conference on Permafrost. International Permafrost Association, Yellowknife, Canada.
Montjuvent, G., Winistörfer, J., 1980. Glaciers quaternaires dans les Alpes franco-suisses et leur piedmont. Géologie Alpine 56, 251–282.
Mottaghy, D., Rath, V., 2006. Latent heat effects in subsurface heat transport modeling and their impact on paleotemperature reconstructions. Geophysical Journal International 164, 236–245.
Muller, S.D., Nakagawa, T., De Beaulieu, J.L., Court-Picon, M., Carcaillet, C., Miramont, C., Roiron, P., Boutterin, C., Ali, A.A., Bruneton, H., 2007. Postglacial migration of silver fir (Abies alba Mill.) in the southwestern Alps. Journal of Biogeography 34, 876–899.
Murton, J.B., Coutard, J.P., Ozouf, J.C., Lautridou, J.P., Robinson, D.A., Williams, R.B.G., 2001. Physical modeling of bedrock brecciation by ice segregation in permafrost. Permafrost and Periglacial Processes 12, 255–266.
Murton, J.B., Peterson, R., Ozouf, J.C., 2006. Bedrock fracture by ice segregation in cold regions. Science 314, 1127–1129.
Noetzli, J., Gruber, S., 2009. Transient thermal effects in Alpine permafrost. The Cryosphere 3, 85–99.
Ortu, E., Peyron, O., Bordon, A., De Beaulieu, J.L., Siniscalco, C., Caramiello, R., 2008. Lateglacial and Holocene climate oscillations in the South-Western Alps: An attempt at quantitative reconstruction. Quaternary International 190, 71–88.
Owen, L.A., Thackray, G., Anderson, R.S., Briner, J., Kaufman, D., Roe, G., Pfeffer, W., Yi, C.L., 2009. Integrated research on mountain glaciers: current status, priorities and future prospects. Geomorphology 103, 158–171.
Prager, C., Ivy-Ochs, S., Ostermann, M., Synal, H.A., Patzelt, G., 2009. Geology and radiometric ^{14}C-, ^{36}Cl- and Th-/U-dating of the Fernpass rockslide (Tyrol, Austria). Geomorphology 103, 93–103.
Riseborough, D.W., Smith, M.W., 1998. Exploring the limits of permafrost, paper presented at 7th International Conference on Permafrost. International Permafrost Association, Yellowknife, Canada.
Riseborough, D., Shiklomanov, N., Etzelmüller, B., Gruber, S., Marchenko, S., 2008. Recent advances in permafrost modeling. Permafrost and Periglacial Processes 19, 137–156.
Safanda, J., 1999. Ground surface temperature as a function of slope angle and slope orientation and its effect on the subsurface temperature field. Tectonophysics 306, 367–375.
Sanchez, G., Rolland, Y., Corsini, M., Braucher, R., Bourlès, D., Arnold, M., Aumaître, G., 2010. Relationships between tectonics, slope instability and climate change: cosmic ray exposure dating of active faults, landslides and glacial surfaces in the SW Alps. Geomorphology 117, 1–13.
Smith, M.W., Riseborough, D.W., 1996. Permafrost monitoring and detection of climate change. Permafrost and Periglacial Processes 7, 301–309.
Stacey, F.D., Davis, P.M., 2008. Physics of the Earth, 4th edition. Cambridge University Press, Cambridge.
van der Beek, P., Bourbon, P., 2008. A quantification of the glacial imprint on relief development in the French western Alps. Geomorphology 97, 52–72.
Vengeon, J.M., 1998. Déformation et rupture des versants en terrain métamorphique anisotrope. Apport de l'étude des ruines de Séchilienne. (PhD thesis) Université Grenoble I, Grenoble (186 pp.).
Wegmann, M., Gudmundsson, G.H., Haeberli, W., 1998. Permafrost changes in rock walls and the retreat of Alpine glaciers — thermal modelling approach. Permafrost and Periglacial Processes 9, 23–33.
Williams, P.J., Smith, M.W., 1989. The Frozen Earth: Fundamentals of Geocryology. Cambridge University Press, Cambridge.